Enhancing the reversible capacity and rate performance of anatase TiO₂ by combined coating and compositing with N-doped carbon

Tao Li [a], Ning Lun [a], Yong-Xin Qi [a], Cheng Wei [a], Yun-Kai Sun [a], Hui-Ling Zhu [b], Jiu-Rong Liu [a, *], Yu-Jun Bai [a, *]

[a] Key Laboratory for Liquid–Solid Structural Evolution and Processing of Materials (Ministry of Education), Shandong University, Jinan 250061, People's Republic of China
[b] School of Materials Science and Engineering, Shandong University of Science and Technology, Qingdao 266590, People's Republic of China

HIGHLIGHTS

- Anatase TiO₂ coated and composited with N-doped carbon was simply fabricated.
- Acrylonitrile can be used as a carbon source to obtain N-doped carbon.
- TiO₂@C composite exhibits markedly improved electrochemical performance.

ARTICLE INFO

ABSTRACT

Anatase TiO₂ nanostructure coated and composited with N-doped carbon was simply fabricated by using acrylonitrile as carbon source. The carbon-coated composite with the TiO₂ nanoparticles dispersed uniformly in the carbon matrix exhibits a high reversible capacity of 223.7 mAh g⁻¹ after cycling 100 times at 100 mA g⁻¹, excellent cycling stability and superior high rate performance (243.5, 219.0, 198.5, 175.8, 153.4 and 130.9 mAh g⁻¹ at 100, 200, 400, 800, 1600 and 3200 mA g⁻¹, respectively) when the carbonization temperature is around 550 °C. The synergistic effect of the combined coating and compositing the N-doped carbon is responsible for the outstanding electrochemical performance.

1. Introduction

One of the key factors for lithium-ion batteries (LIBs) with high energy density, high power density, and long cycling life applicable in electric vehicles (EV) and hybrid electric vehicles (HEV) is to find appropriate anode materials. Li₄Ti₅O₁₂ (LTO) has a spinel structure [1], which exhibits negligible structural change during charging-discharging [2], long-term cycling stability, good high-rate performance, and a wide voltage plateau around 1.55 V with enhanced safety, thus could be a promising anode materials for electric vehicles. However, the inherently insulating nature of LTO seriously hinders the high rate performance. Doping with heterogenous ions has been demonstrated to be an effective method to improve the electrochemical performance [3–8]. TiO₂ is another anode material

with the similar merits to LTO, and the prominent advantages over LTO lie in the lower cost owing to the absence of lithium, lower energy consumption due to the low sintering temperature, and the higher theoretical capacity (335 mAh g⁻¹ for TiO₂ and 175 mAh g⁻¹ for LTO). Among the various polymorphs of TiO₂, anatase and TiO₂–B (a monoclinic metastable phase of TiO₂) have been extensively investigated as potential anode materials for LIBs due to their open channel structure and high insertion capacity in comparison with rutile TiO₂ [9–13]. However, the intrinsically low Li-ion diffusivity (10⁻¹⁵–10⁻⁹ cm² s⁻¹) and electronic conductivity (10⁻¹²–10⁻⁷ S cm⁻¹) of TiO₂ deteriorate the reversible capacity and rate capability [14,15]. As a consequence, various TiO₂ nanostructures with large surface area and reduced size such as nanotubes [16–18], nanowires [19], nanospheres [9,20] and nanosheets [21], have been prepared to reduce the Li-ion diffusion pathway and increase the contact area between electrode material and electrolyte. The nanostructures contribute to the fast Li⁺ insertion/extraction reactions, and thus exhibit significantly improved rate

* Corresponding authors. Tel./fax: +86 531 88392315.
  E-mail addresses: jrliu@sdu.edu.cn (J.-R. Liu), byj97@126.com (Y.-J. Bai).

performance and cycling stability relative to the bulk particles despite the intrinsically low electronic and ionic conductivity. So far, the nanostructured TiO_2 were commonly prepared by complex methods (such as using templates) and multiple steps but with low yield, unfavorable for large-scale production in industry.

As has been proven, coating carbon on the surface of electrode materials could effectively improve the electrochemical performance by virtue of enhancing the electronic conductivity and preventing nanoparticles from agglomeration [22–27]. In particular, the N-doped carbon (including graphene) exhibits more superiority than the pure carbon in enhancing the electronic conductivity, ion permeability of the carbon layer and charge transfer at the interface of the metal oxide/carbon hybrids or composite, thus could significantly improve the reversible capacity and rate capability, as have been demonstrated in the literature [22,28–30]. However, to date, the research on TiO_2 is dominantly focused on TiO_2–B and only a few reports are concerning with the Li-ion storage performance of carbon-coated anatase TiO_2 (A-TiO_2), because TiO_2–B has a more open structure than A-TiO_2 [31–33]. Meanwhile, the low reversible capacity of A-TiO_2 (about 185 mAh g^{-1} which is lower than 372 mAh g^{-1} for graphite) is a factor restricting its application in LIBs. How to obtain A-TiO_2 with high capacity and rate performance is of great significance for using as anode materials in LIBs.

In this work, we prepared A-TiO_2 nanostructure with combined N-doped carbon coating and compositing by a simple two-step process using tetrabutyl titanate (TBT) as starting material and a general chemical reagent of acrylonitrile (AN) as carbon source. Compared with the method using polydopamine (PODA) as the carbon precursor to form carbon coating on TiO_2 nanoparticles [33], the method in this work is easy and time-saving, and the carbon source of AN is more available and cheaper. In particular, the carbon-coated composite exhibits enhanced reversible capacity, excellent cycling stability and high rate performance as the anode material for LIBs owing to the synergistic effect of the combination of coating and compositing with the N-doped carbon.

2. Experimental

2.1. Material preparation

All chemicals involved are of analytical pure grade and were used without further purification. The preparation of TiO_2@C composite includes two steps. (1) A solution containing 50 mL ethanol and 0.1 mol tetrabutyl titanate (TBT) was added dropwise into 10 mL distilled water under magnetic stirring at ambient temperature. The hydrolysis of TBT can be expressed as: $Ti(C_4H_9O)_4 + 4H_2O \rightarrow Ti(OH)_4 + 4C_4H_9OH$. Porous TiO_2 was obtained by drying the precipitate in an oven at 120 °C for 3 h and another 2 h at 250 °C in air. (2) A rapid carbon coating method was adopted by putting 1.5 g TiO_2 into a stainless steel autoclave of 30 mL in capacity and uniformly dropping 0.55 mL AN into the powder by a needle tubing, followed by heating the tightly sealed autoclaves at 550 °C for 5 h in a muffle furnace. When the autoclave was cooled naturally to ambient temperature, the black powder collected is denoted as TiO_2@C-550. As a comparison, the product obtained at a carbon coating temperature of 600 °C is assigned to TiO_2@C-600. The formation of TiO_2@C composite includes thermal polymerization of AN into polyacrylonitrile (PAN) around the TiO_2 nanoparticles and subsequent pyrolysis of the PAN into N-doped carbon.

2.2. Characterization

X-ray diffraction (XRD) patterns were obtained on a Rigaku Dmax-rc diffractometer with Ni filtered CuKα radiation (V = 40 kV,

I = 50 mA) at a scanning rate of 4° min^{-1}. The morphology of the products was examined using a JEOL JEM-2100 high-resolution transmission electron microscope (HRTEM). X-ray photoelectron spectra (XPS) were analyzed on a KARTOS XSAM800 X-ray photoelectron spectrometer (Kratos Analytical Ltd., Manchester, U.K.) using Al Kα radiation (hv = 1486.6 eV) as the excitation source (V = 12 kV, I = 10 mA). The electronic conductivity of the products was measured in an Ecopia HMS-3000 Hall effect measurement system by pressing the powder into thin plates under a pressure of 20 MPa. Thermogravimetric (TG) analysis was performed from ambient temperature to 800 °C in air at a heating rate of 10 °C min^{-1} using an SDT thermal-microbalance apparatus to evaluate the carbon content. Raman spectra were collected on a Lab-RAM HR800 with excitation from an argon ion laser (632.81 nm). Nitrogen adsorption and desorption isotherms were carried out at 77 K on a Quadrasorb SI sorption analyzer. The samples were degassed at 300 °C for 3 h under a vacuum in the degas port of the analyzer. The specific surface area was calculated with the Brunauer–Emmett–Teller (BET) model, and the pore-size distribution was calculated from the adsorption/desorption data by using the Density Functional Theory (DFT) method.

2.3. Electrochemical measurements

CR2025 coin-type cells were assembled in an argon-filled glove box using Li metal as the counter and reference electrodes. The working electrodes were composed of 80 wt% TiO_2 or TiO_2@C, 10 wt% acetylene black as conducting agent, and 10 wt% polyvinylidene fluoride (PVDF) as binder. The uniform slurry after mechanically stirring was coated on thin Cu foils, and dried in a vacuum oven for 12 h at 120 °C. A Celgard 2300 membrane was used as the separator. The electrolyte consists of the solution of 1 M LiPF$_6$ in a 1:1 (v/v) EC/DMC. The weight of active material loaded on each disk (14 mm in diameter, punched from the Cu foils) is around 3.0 mg. The cells were galvanostatically discharged and charged at varied current densities in the voltage range from 0.02 V to 3.0 V (vs. Li/Li$^+$) on a Land CT2001A battery test system at 25 °C. Cyclic voltammograms (CV) were measured on an IviumStat electrochemistry workstation over the potential range of 0.01–3.0 V vs. Li/Li$^+$ at a scanning rate of 0.1 mV s^{-1}, and electrochemical impedance spectra (EIS) were tested with an ac signal amplitude of 5 mV in the frequency range from 100 kHz to 0.1 Hz.

3. Results and discussion

The morphology and structure of the products was examined by TEM, as shown in Fig. 1. From Fig. 1a, the as-obtained TiO_2@C-550 exhibits a porous spherical structure (similar to the uncoated TiO_2 displayed in Fig. S1 of Supporting Information (SI)) with the TiO_2 nanoparticles (about 6–18 nm in diameter) dispersed uniformly in the carbon matrix. The diameters of the porous TiO_2@C spheres are in the range of 80–160 nm. The strong diffraction rings in the corresponding electron diffraction pattern (EDP) revealed in the inset of Fig. 1a can be indexed to the (101), (004), (200), and (105) planes of A-TiO_2 from inside to outside, demonstrating the high crystallization of A-TiO_2. From the high magnification image in Fig. 1b, besides the thin carbon layer in amorphous form around the TiO_2 nanoparticles, amorphous carbon is filled among the nanoparticles as pointed out by black arrows, demonstrating the combination of carbon coating and compositing with A-TiO_2. The lattice fringes with a spacing of 0.35 nm corresponds to the (101) plane of A-TiO_2. For TiO_2@C-600 (Fig. 1c and d), the morphology is analogous to that in TiO_2@C-550, but the diameters of the porous spheres and the encapsulated nanoparticles are in the range of 100–220 nm and 9–20 nm, respectively, slightly larger than those in TiO_2@C-
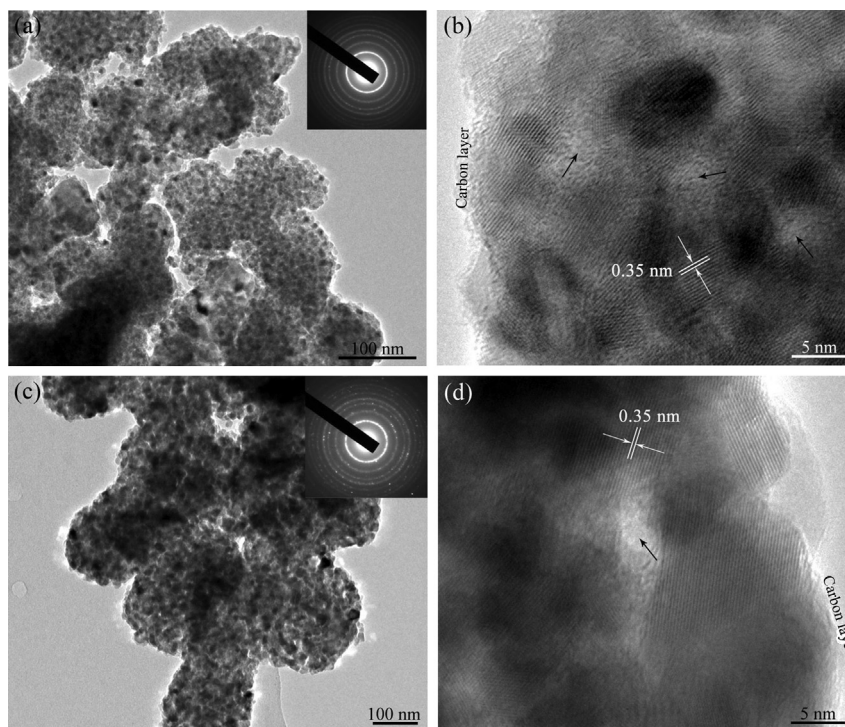
Fig. 1. TEM images of TiO$_2$@C-550 (a, b) and TiO$_2$@C-600 (c, d). The insets in (a) and (c) are the corresponding EDPs.

550, and the carbon layer is thinner than that of TiO$_2$@C-550. The porous structure comprised of carbon-coated TiO$_2$ nanoparticles is conducive to electrolyte permeation, Li-ion diffusion and electron transport when utilized as anode materials, thus could provide enhanced lithiation/delithiation performance [9,10].

In the XRD patterns (Fig. 2), the diffraction peaks of the as-prepared TiO$_2$ could be well indexed to those from A-TiO$_2$ (JCPDS card No. 21-1272), and the diffractions of TiO$_2$@C-550 are similar to the pristine A-TiO$_2$, while some weak diffractions from rutile TiO$_2$ (JCPDS card No. 21-1276) appear in the XRD pattern of TiO$_2$@C-600 due to the phase transformation from anatase to rutile TiO$_2$ occurring around 600 °C [34]. No detectable peaks from carbon could be distinguished in the products, confirming the amorphous nature of the carbon in the TiO$_2$@C composites. After coating carbon, the diffraction peaks of TiO$_2$ become sharper owing to the enhanced crystallization at higher temperature of 550 and 600 °C than the sintering temperature (250 °C). The average crystallite sizes calculated by the Scherrer equation are approximately 12.1 nm for TiO$_2$@C-550, 15.6 nm for TiO$_2$@C-600 and 5.8 nm for TiO$_2$.

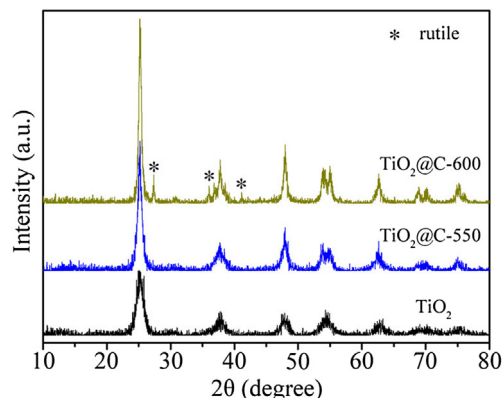The carbon structure in the TiO$_2$@C composites was determined by Raman spectra, as shown in Fig. S2 of the SI. The two characteristic peaks located at about 1360 and 1592 cm^{-1} correspond to the D-band and G-band of carbon materials, respectively, and the intensity ratio of them (0.87 for TiO$_2$@C-550 and 0.75 for TiO$_2$@C-600) suggests the existence of disorder carbon, consistent with the XRD and TEM results. The higher coating temperature could result in the slightly higher graphitization degree of carbon in TiO$_2$@C-600 than that in TiO$_2$@C-550.

The porous nature of the as-prepared TiO$_2$ and TiO$_2$@C composites could be confirmed by the nitrogen absorption/desorption isotherms, as revealed in Fig. S3 of the SI. The typical IV-type curve denotes the presence of mesopores in the as-prepared TiO$_2$ and TiO$_2$@C nanostructures. The specific surface area calculated with the BET model is 181.1 m^2 g^{-1} for TiO$_2$, 26.8 m^2 g^{-1} for TiO$_2$@C-550 and 61.7 m^2 g^{-1} for TiO$_2$@C-600. The decrease in specific surface area after coating carbon at higher temperatures of 550 and 600 °C is due to the slight growth of crystallite size (as evidenced by XRD and TEM), especially some pores were filled with carbon. From the pore size distribution curve in the inset of Fig. S3a and b, the pores with detectable sizes of 2.0, 2.8 and 4.7 nm presents in TiO$_2$@C-550, and a wider pore-size distribution with an average pore size of 8.2 nm in TiO$_2$@C-600, indicating the enlarged pores in the TiO$_2$@C nanostructures at the higher carbon coating temperature. For the as-sintered TiO$_2$ without coating carbon, the pore size is mainly of 4.0 nm, as shown in the inset of Fig. S3c. Noted that TiO$_2$@C-600 has a higher specific surface area but a higher pore size than TiO$_2$@C-550, because treatment conditions are the same except for the different heating temperatures, the difference in specific surface area could be ascribed to the larger shrinkage of carbon at 600 °C than at 550 °C due to the enhanced graphitization degree and the lower carbon content resulted from enhanced pyrolysis degree of PAN at a higher temperature.

To confirm the formation of N–doped carbon, XPS was adopted to determine the chemical composition of the TiO$_2$@C composites. From the survey spectra (Fig. 3a), in addition to the dominant

Fig. 2. XRD patterns of the as-sintered TiO$_2$, TiO$_2$@C-550 and TiO$_2$@C-600.

elements of Ti, O and C, N could also be detected, verifying the formation of N-doped carbon materials. From the deconvoluted N1s spectra in Fig. 3b, the peaks around 398.8 and 400.2 eV are resulted from pyridinic and pyrrolic N in carbon materials, respectively [35,36], and the intensity of N1s peak in TiO$_2$@C-550 is more intense than that in TiO$_2$@C-600 owing to the denitrification at higher temperature. Meanwhile, the carbon coating temperature also leads to the difference in the pyridinic and pyrrolic N in the two products. The atomic content of nitrogen determined by the XPS result is 5.4 at% for TiO$_2$@C-550 and 1.5 at% for TiO$_2$@C-600. The C1s spectra displayed in Fig. 3c could be fitted to three peaks, the strong one at 285.0 eV belongs to graphitic carbon [37], the weak one at 286.8 eV to disordered carbon or oxidant carbon [37,38], and the other weak one at 289.2 eV to trace amount of carboxyl in the products [37].

As has been reported [28–30,39,40], the N-doped carbon could effectively improve the electrochemical performance of electrode materials owing to the enhancement in electronic conductivity and charge transfer at the interfaces. The electronic conductivity measured is 5.80×10^{-11} S cm^{-1} for the as-sintered TiO$_2$, 9.96×10^{-8} S cm^{-1} for TiO$_2$@C-550 and 3.68×10^{-8} S cm^{-1} for TiO$_2$@C-600, increasing approximately by three orders of magnitude owing to the N-doped carbon coating and compositing with A-TiO$_2$. To evaluate the carbon content in the products, TG analysis was carried out, as shown in Fig. S4 of the SI. The tiny weight loss below 150 °C is attributed to the evaporation of the absorbed moisture, and the main weight loss at about 400 °C to the oxidation of carbon, giving rise to a weight loss of 12.6 wt% for TiO$_2$@C-550 and 3.1 wt% for TiO$_2$@C-600. The difference in carbon content is owing to the pyrolysis degree of PAN at different temperatures.

As a result of the high carbon content in TiO$_2$@C-550 composite, the cells were galvanostatically charged/discharged in the voltage range of 0.02–3.0 V (vs. Li/Li$^+$) rather than the commonly used 1.0–3.0 V as reported, and the cells of TiO$_2$@C-600 and TiO$_2$ were measured under the same condition for comparison. The charge/

discharge curves of the TiO$_2$ and TiO$_2$@C cells for the initial four cycles are displayed in Fig. 4a, c and e. The voltage profiles of the first cycle for the three products exhibit a discharge voltage plateau at ~1.7 V and a charge plateau at ~2.0 V, which are the typical characteristic of A-TiO$_2$ during charging/discharging. From Fig. 4a, the as-sintered TiO$_2$ delivers a discharge capacity of 169.8 and a charge capacity of 145.6 mAh g^{-1}, corresponding to a Coulombic efficiency of 85.8%. After coating carbon (Fig. 4c and e), though the Coulombic efficiency of the first cycle is lower than that of the as-sintered TiO$_2$ (68.3% for TiO$_2$@C-550 and 54.5% for TiO$_2$@C-600), the first discharge capacity is as high as 337.6 mAh g^{-1} for TiO$_2$@C-550 and 306.7 mAh g^{-1} for TiO$_2$@C-600 because of the different carbon contents and graphitization degrees of the two products. The large irreversible capacities during the first cycle are 107.1 mAh g^{-1} for TiO$_2$@C-550 and 139.4 mAh g^{-1} for TiO$_2$@C-600, resulting in low initial Coulombic efficiency of 68.3% and 54.5%, respectively. Generally, the larger specific surface area leads to the lower initial Coulombic efficiency due to the more side reactions involving lithium intercalation into trapped sites [41]. It is true for TiO$_2$@C-550 and TiO$_2$@C-600 with the specific surface areas of 26.8 and 61.7 m^2 g^{-1}, respectively. However, it is not the case for the as-sintered TiO$_2$ in this work though it possesses the highest specific surface area of 181.1 m^2 g^{-1} among the three samples, the initial Coulombic efficiency is 85.8%, higher than that of TiO$_2$@C-550 and TiO$_2$@C-600, because it delivers a low initial capacity of 169.8 mAh g^{-1} (much lower than 337.6 mAh g^{-1} for TiO$_2$@C-550 and 306.7 mAh g^{-1} for TiO$_2$@C-600) during the first discharging for lack of carbon in comparison with the TiO$_2$@C electrodes tested in the same voltage range of 0.02–3.0 V. The charge/discharge curves in the subsequent cycles almost overlap with the second one, implying the good cycling performance of the TiO$_2$@C composites. Furthermore, a small plateau appears at ~0.6 V during the first discharging of TiO$_2$@C-550, however, it is not obvious for TiO$_2$@C-600 due to the lower carbon content in the product. The plateau can be attributed to the formation of solid electrolyte interface (SEI) films on the surface of carbon [9,42].
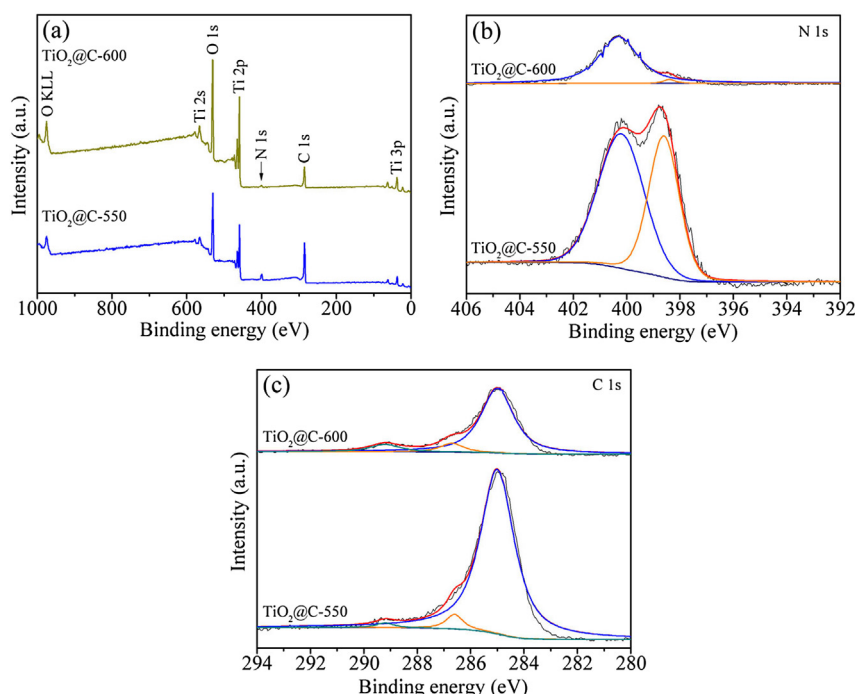

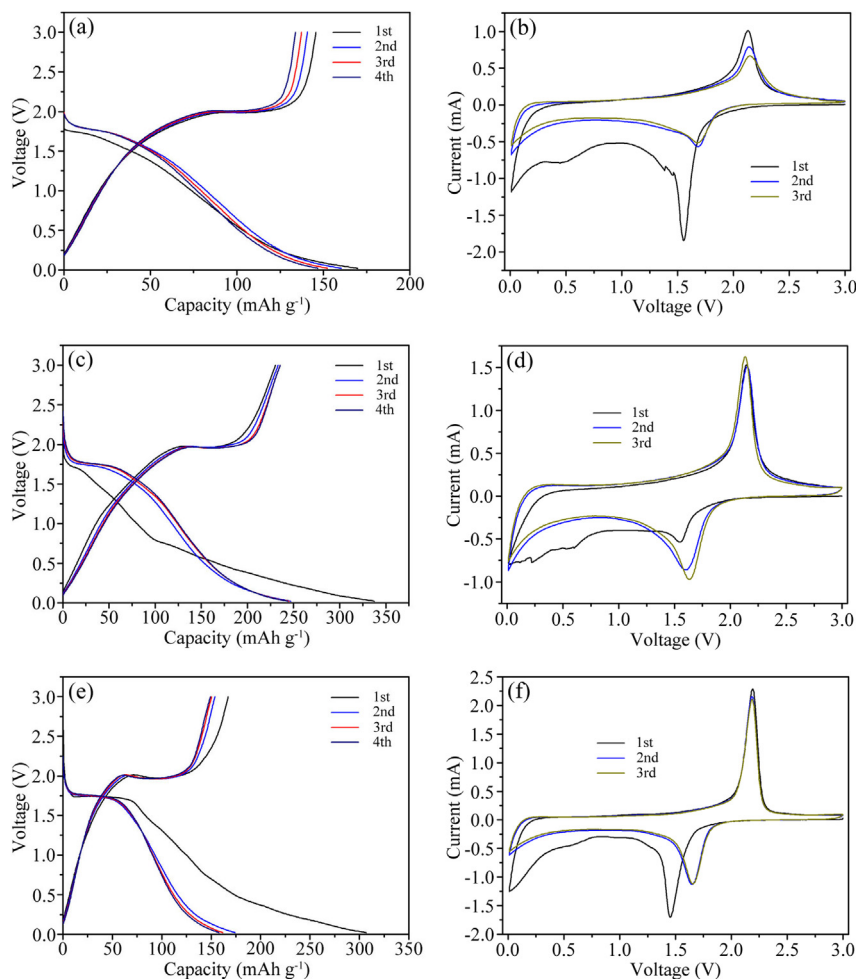**Fig. 3.** XPS spectra of TiO$_2$@C-550 and TiO$_2$@C-600. (a) Survey spectra, (b) N1s and (c) C1s spectra.

Fig. 4. Galvanostatic charge/discharge curves at 100 mA g^{-1} and CV profiles at a scanning rate of 0.1 mV s^{-1} for TiO$_2$ (a, b), TiO$_2$@C-550 (c, d) and TiO$_2$@C-600 (e, f).

The CV profiles of the cells for the first three cycles were carried out at a scan rate of 0.1 mV s^{-1} in the voltage range of 0.01–3.0 V and are presented in Fig. 4b, d and f. As can be seen, the CV curve of the first cycle clearly shows a pair of cathodic/anodic peaks at ~1.5 V and 2.1 V, corresponding to the lithium ion insertion into and extraction out of the active materials, respectively. From the second cycle, the cathodic/anodic peaks stabilize at ~1.7 V and 2.1 V, and the redox peaks of the TiO$_2$@C electrodes are sharp and intense relative to that of the TiO$_2$ electrodes. In addition, the CV profile for the first cycle is different from the subsequent ones and a weak peak at ~0.6 V can be observed during the first cathodic scan owing to the formation of SEI films on the surface of the active materials [9,37,42]. These CV results reflect well with the charge/discharge curves.

Fig. 5a reveals the cycling performance at a current density 100 mA g^{-1}. It is obvious, the first discharge capacity of the carbon-coated TiO$_2$ is much higher than that of the as-sintered one, meanwhile, the TiO$_2$@C composites exhibit significantly improved cycling stability. After 100 cycles, the discharge capacity of the as-sintered TiO$_2$ declines to 82.4 mAh g^{-1}, however, TiO$_2$@C-600 could retain a reversible capacity of 140.1 mAh g^{-1} with the Coulombic efficiency close to 100%, in particular, TiO$_2$@C-550 delivers a reversible capacity of 223.7 mAh g^{-1}, higher than the practical reversible capacity of A-TiO$_2$ (~185 mAh g^{-1} in the range of 1.0–3.0 V). Apparently, the N-doped carbon plays a key role in improving the cycling performance owing to the enhanced

electronic conductivity, and the elastic and good mechanical stability [33,36,43]. The lower capacity of TiO$_2$@C-600 than TiO$_2$@C-550 could be ascribed to the lower electronic conductivity due to the lower nitrogen content, lower carbon content owing to the more fully pyrolysis of PAN, larger crystallite size and the presence of a trace amount of rutile TiO$_2$ in TiO$_2$@C-600 because of the smaller diffusion coefficient of Li-ions in rutile TiO$_2$ than that in A-TiO$_2$ [44].

High rate performance is one of the significant electrochemical aspects for LIBs especially for high-power applications such as HEV and EV. The rate capabilities were tested at various current densities each for 10 cycles, as shown in Fig. 5b. The reversible capacities for TiO$_2$@C-550 are 243.5, 219.0, 198.5, 175.8, 153.4 and 130.9 mAh g^{-1} at 100, 200, 400, 800, 1600 and 3200 mA g^{-1}, respectively, and those for TiO$_2$@C-600 are 164.8, 135.7, 115.7, 94.5, and 69.6 mAh g^{-1} at 100, 200, 400, 800, and 1600 mA g^{-1}, respectively, indicating that the electronic conductivity plays a key role in high rate performance rather than the specific surface area. The cycling performance of the TiO$_2$@C was also measured at a current density of 500 mA g^{-1} without low-rate activation, as shown in Fig. 5c. After 200 cycles, TiO$_2$@C-550 could deliver an outstanding reversible capacity of 180.9 mAh g^{-1} (corresponding to a capacity retention of 83.9%), while the TiO$_2$@C-600 retains a capacity of 119.7 mAh g^{-1} (corresponding to a capacity retention of 76.1%), confirming the better cycling stability of TiO$_2$@C-550 than TiO$_2$@C-600 even at a higher current density.
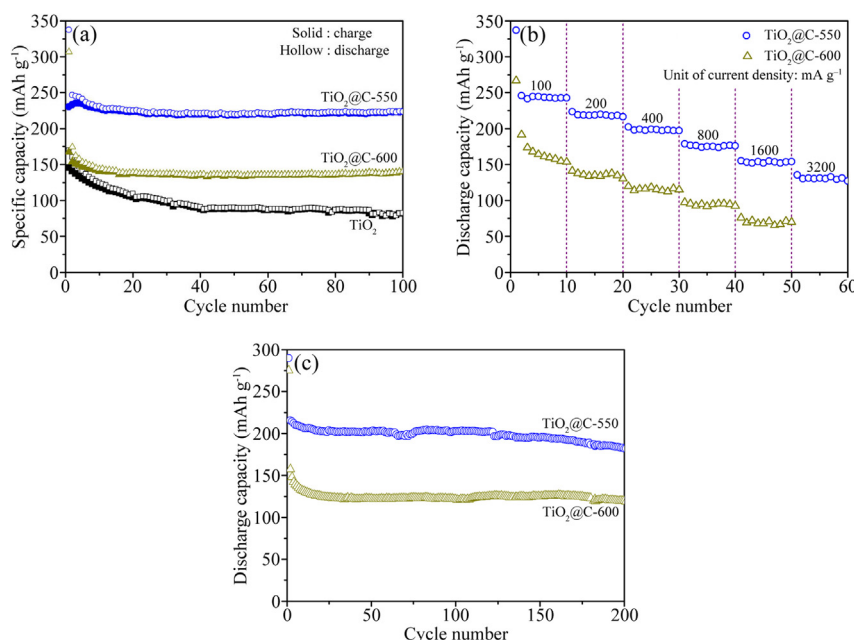
Fig. 5. (a) Cycling performance of TiO$_2$, TiO$_2$@C-550 and TiO$_2$@C-600 at 100 mA g^{-1}, (b) rate performance, and (c) cycling performance at 500 mA g^{-1} without low-rate activation.

The difference in electrochemical performance associates greatly with the electronic conductivity, so EIS were measured to compare the charge transfer resistance and Li-ion diffusion kinetics, as displayed in Fig. 6. From Fig. 6a, the spectra exhibits a semicircle in the high and medium frequency region followed by an inclined line in the low frequency region. The TiO$_2$@C cells exhibit smaller semicircle diameter, indicative of the higher electronic conductivity than the TiO$_2$ cells. Fig. 6b depicts the equivalent circuit fitting to the EIS, where R_s is the ohmic resistance from electrolyte, R_{SEI}, the resistance for Li$^+$ migration through the SEI film, R_{ct}, the charge transfer resistance, and Z_w, the Warburg impedance associated with Li-ion diffusion kinetics [45,46]. The constant phase elements (CPE) replace pure capacitance in this model. From the simulated equivalent circuit, the charge transfer resistances determined are 230 ± 7 Ω for TiO$_2$, 27 ± 2 Ω for TiO$_2$@C-550, and 85 ± 3 Ω for TiO$_2$@C-600, demonstrating that the N-doped carbon indeed improves the electronic conductivity and charge transfer at the

interfaces. The value of R_{ct} is in the order of TiO$_2$@C-550 < TiO$_2$@C-600 < TiO$_2$, in good agreement with the electrochemical performance obtained above. Furthermore, the lower resistance of TiO$_2$@C-550 than TiO$_2$@C-600 is associated with the higher nitrogen content in TiO$_2$@C-550 than that in TiO$_2$@C-600, as determined by XPS.

The high reversible capacity, excellent cycling stability and superior high rate performance of the TiO$_2$@C-550 composite make it a promising candidate as anode material for high-performance LIBs. Such pronounced electrochemical performance could be ascribed to several beneficial features. (1) The porous nanostructure of TiO$_2$@C-550 with relatively high specific surface area is conducive to improving the wettability of the electrolyte to active material, increasing the electrode/electrolyte contact interface and shortening the transport distance for Li-ion diffusion, thus favorable for the rate capability [9,10]. (2) The amorphous carbon matrix could endow the TiO$_2$@C both elastic and good mechanical stability during cycling, conducive to the enhanced capacity retention [33,43]. (3) Most importantly, the N-doped carbon could significantly enhance the electronic conductivity and facilitate fast Li$^+$ ion transport and electrochemical reaction dynamics, contributing to the Li-ion storage and high rate performance [28–30,33,36,39,40]. (4) The more carbon content (both coating on the TiO$_2$ nanoparticles and fitting in the pores) in the product is responsible for the higher capacity. As a consequence, the outstanding electrochemical performance of TiO$_2$@C-550 results from the synergistic effect of the combined coating and compositing with the N-doped carbon to form the porous structure.

4. Conclusions

In summary, the porous anatase TiO$_2$ coated and composited with N-doped carbon could be simply fabricated using the general chemical reagent of AN as the carbon source. The composite prepared at 550 °C exhibits high reversible capacity, excellent cycling stability and high rate performance owing to the enhanced electronic conductivity. The superior electrochemical performance of TiO$_2$@C-550 allows it applicable as anode material for high performance LIBs requiring high-power densities.
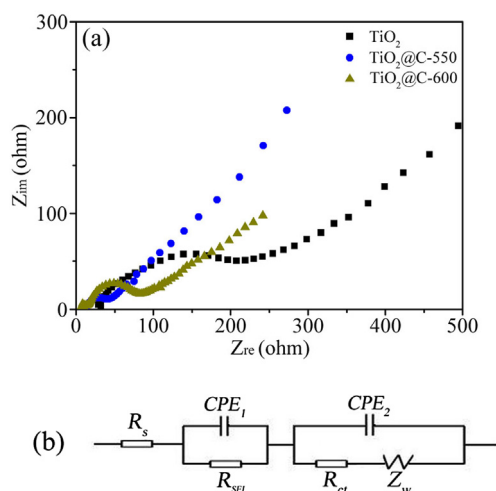

Fig. 6. (a) Impedance spectra of TiO$_2$, TiO$_2$@C-550 and TiO$_2$@C-600 cells after 100 cycles, (b) equivalent circuit fitting to the EIS.

Acknowledgments

Appendix A. Supplementary data

Supplementary data related to this article can be found at http://dx.doi.org/10.1016/j.jpowsour.2014.09.107.

References

[1] K.M. Colbow, J.R. Dahn, R.R. Haering, J. Power Sources 26 (1989) 397.
[2] K. Ariyoshi, R. Yamato, T. Ohzuku, Electrochim. Acta 51 (2005) 1125.
[3] Y.J. Bai, C. Gong, Y.X. Qi, N. Lun, J. Feng, J. Mater. Chem. 22 (2012) 19054.
[4] T.F. Yi, Y. Xie, L.J. Jiang, J. Shu, C.B. Yue, A.N. Zhou, M.F. Ye, RSC Adv. 2 (2012) 3541.
[5] B. Zhang, Z.D. Huang, S. Oh, J.K. Kim, J. Power Sources 196 (2011) 10692.
[6] Z. Yu, X. Zhang, G. Yang, J. Liu, J. Wang, R. Wang, J. Zhang, Electrochim. Acta 56 (2011) 8611.
[7] Y.J. Bai, C. Gong, N. Lun, Y.X. Qi, J. Mater. Chem. A 1 (2013) 89.
[8] T.F. Yi, H. Liu, Y.R. Zhu, L.J. Jiang, Y. Xie, R.S. Zhu, J. Power Sources 215 (2012) 258.
[9] H.E. Wang, H. Cheng, C.P. Liu, X. Chen, Q.L. Jiang, Z.G. Lu, J. Power Sources 196 (2011) 6394.
[10] K. Saravanan, K. Ananthanarayanan, P. Balaya, Energy Environ. Sci. 3 (2010) 939.
[11] S.H. Liu, Z.Y. Wang, C. Yu, H.B. Wu, G. Wang, Adv. Mater. 25 (2013) 3462.
[12] H.S. Liu, Z.H. Bi, X.G. Sun, R.R. Unocic, M.P. Paranthaman, S. Dai, Adv. Mater. 23 (2011) 3450.
[13] G. Armstrong, A.R. Armstrong, J. Canales, P.G. Bruce, Chem. Commun. 19 (2005) 2454.
[14] D.V. Bavykin, J.M. Friedrich, F.C. Walsh, Adv. Mater. 18 (2006) 2807.
[15] S. Bach, J.P. Pereira-Ramos, P. Willman, Electrochim. Acta 55 (2010) 4952.
[16] J. Kim, J. Cho, J. Electrochem. Soc. 154 (2007) A542.
[17] K.X. Wang, M.D. Wei, M.A. Morris, H.S. Zhou, J.D. Holmes, Adv. Mater. 19 (2007) 3016.
[18] M. Plylahan, M. Letiche, M.K.S. Barr, T. Djenizian, Electrochem. Commun. 43 (2014) 121.
[19] Y.M. Li, X.J. Lv, J.H. Li, Appl. Phys. Lett. 95 (2009) 113102.
[20] M. Sasidharan, K. Nakashima, N. Gunawardhana, T. Yokoi, M. Inoue, S. Yusa, Chem. Commun. 47 (2011) 6921.
[21] B. Hao, Y. Yan, X.B. Wang, G. Chen, ACS Appl. Mater. Interfaces 5 (2013) 6285.
[22] C. Gong, Y.J. Bai, J. Feng, R. Tang, Y.X. Qi, N. Lun, R.H. Fan, ACS Appl. Mater. Interfaces 5 (2013) 4209.
[23] W.M. Zhang, X.L. Wu, J.S. Hu, Y.G. Guo, L.J. Wan, Adv. Funct. Mater. 18 (2008) 3941.
[24] Y.H. Jin, S.D. Seo, H.W. Shim, K.S. Park, D.W. Kim, Nanotechnology 23 (2012) 125402.
[25] M.M. Zhen, X.J. Guo, G.D. Gao, Z. Zhou, L. Liu, Chem. Commun., http://dx.doi.org/10.1039/c4cc05480f.
[26] L.W. Su, Y. Jing, Z. Zhou, Nanoscale 3 (2011) 3967.
[27] M.M. Zhen, L.W. Su, Z.H. Yuan, L. Liu, Z. Zhou, RSC Adv. 3 (2013) 13696.
[28] C. Lei, F. Han, D. Li, W.C. Li, Q. Sun, X.Q. Zhang, A.H. Lu, Nanoscale 5 (2013) 1168.
[29] C. Gong, Y.J. Bai, Y.X. Qi, N. Lun, J. Feng, Electrochim. Acta 90 (2013) 119.
[30] D.D. Cai, D.D. Li, S.Q. Wang, X.F. Zhu, W.S. Yang, S.Q. Zhang, H.H. Wang, J. Alloys Compd. 561 (2013) 54.
[31] S.J. Park, H. Kim, Y.J. Kim, H. Lee, Electrochim. Acta 56 (2011) 5355.
[32] B. Oschmann, D. Bresser, M.N. Tahir, K. Fischer, W. Tremel, S. Passerini, Macromol. Rapid Commun. 34 (2013) 1693.
[33] L. Tan, L. Pan, C.Y. Cao, B.F. Wang, L. Li, J. Power Sources 253 (2014) 193.
[34] V.G. Pol, A. Zaban, Langmuir 23 (2007) 11211.
[35] Z.S. Wu, W.C. Ren, L. Xu, F. Li, H.M. Cheng, ACS Nano 5 (2011) 5463.
[36] T. Li, Y.Y. Wang, R. Tang, Y.X. Qi, N. Lun, Y.J. Bai, R.H. Fan, ACS Appl. Mater. Interfaces 5 (2013) 9470.
[37] Z.X. Yang, G.D. Du, Q. Meng, Z.P. Guo, X.B. Yu, Z.X. Chen, J. Mater. Chem. 22 (2012) 5848.
[38] N. Ohtsu, N. Masahashi, Y. Mizukoshi, K. Wagatsuma, Langmuir 25 (2009) 11586.
[39] L.W. Su, Z. Zhou, P.W. Shen, J. Phys. Chem. C 116 (2012) 23974.
[40] L. Zhao, Y.S. Hu, H. Li, Z.X. Wang, L.Q. Chen, Adv. Mater. 23 (2011) 1385.
[41] J.W. Xu, Y.F. Wang, Z.H. Li, W.F. Zhang, J. Power Sources 175 (2008) 903.
[42] F.D. Han, Y.J. Bai, R. Liu, B. Yao, Y.X. Qi, N. Lun, J.X. Zhang, Adv. Energy Mater. 1 (2011) 798.
[43] Y.G. Guo, J.S. Hu, L.J. Wan, Adv. Mater. 20 (2008) 2878.
[44] J. Ming, Y.Q. Wu, S. Nagarajan, D.J. Lee, Y.K. Sun, F.Y. Zhao, J. Mater. Chem. 22 (2012) 22135.
[45] J.Z. Wang, C. Zhong, D. Wexler, N.H. Idris, Z.X. Wang, L.Q. Chen, H.K. Liu, Chem. Eur. J. 17 (2011) 661.
[46] Q.C. Zhuang, S.D. Xu, X.Y. Qiu, Y.L. Cui, L. Fang, S.G. Sun, Prog. Chem. 22 (2010) 1044.